DESIGN AND CONSTRUCTION OF A PHASE-STEPPING INTERFEROMETER FOR THE STUDY OF THIN FILMS

By

Sean Daigler

A thesis submitted in partial fulfillment of the
requirements for the degree of

Bachelor of Science

Houghton College

July 2015

Signature of Author……………………………………………..…………………..
<div align="right">Department of Physics
July 14, 2015</div>

…………………………………………………………………….………………..
<div align="right">Dr. Brandon Hoffman
Associate Professor of Physics
Research Supervisor</div>

…………………………………………………………………………………………..
<div align="right">Dr. Mark Yuly
Professor of Physics</div>

DESIGN AND CONSTRUCTION OF A PHASE-STEPPING INTERFEROMETER FOR THE STUDY OF THIN FILMS

By

Sean Daigler

Submitted to the Department of Physics
on July 14, 2015 in partial fulfillment of the
requirement for the degree of
Bachelor of Science

Abstract

A phase-stepping laser interferometer is under construction at Houghton College to study thin metal films. A 50 mW, 634 nm laser in combination with a beam splitter and a series of lenses produce 4 in collimated beams of light. Sets of images are taken by a webcam as a reference mirror moves, producing stepped changes in the interference pattern. The series of pictures are analyzed using a LabVIEW program to create a topographical image of the surface which will be a measure of curvature and will allow for calculation of stresses within the film. The interferometer will be mounted under a deposition chamber, where thin metal films are deposited allowing for in-situ imaging.

Thesis Supervisor: Dr. Brandon Hoffman
Title: Associate Professor of Physics

TABLE OF CONTENTS

TABLE OF FIGURES

INTRODUCTION

1.1 Thin Films

1.1.1 Introduction to Thin Films

Thin films are structures that are small in one direction compared to its extent in the other two directions [1]. The material properties of thin film, particularly if it is attached to a substrate, differ significantly from the properties of the bulk material that the film is created from. Abnormal stresses can occur at the interface between the thin film and the substrate due to mismatches in coefficients of thermal expansion amongst other factors [2]. These stresses may result in device failure, thus further research into the stresses within thin films is important.

Thin metal films have a variety of applications in modern engineering systems. They are critical to the continual development in the area of miniaturizing electronic circuitry due to their application in microelectromechanical systems (MEMs) [3]. In addition, thin films are used as protective coatings from high temperature and other intense environments. In high friction systems such as internal combustion engines, artificial joints, and computer hard drives, thin film coatings can lengthen the lifespan of the components [4].

1.1.2 Stresses in Thin Films

Stresses are present within thin films in two main forms, growth stresses and induced stresses. Growth stresses, often referred to as intrinsic stresses, are strongly dependent on the particular material being deposited and the temperature at which the deposition occurs. Intrinsic stress is induced due to surface and interface tensions such as the interface between a film and a substrate, grain growth or grain boundary reduction, impurities within the deposited material, and phase transformations amongst other factors. Induced stresses, often referred to as extrinsic stresses, are stresses induced on a thin film by the environment after growth is complete. Common factors that induce extrinsic stresses include

changes in magnetic forces, changes in electrostatic forces, changes in temperature, inertial forces, chemical reactions and phase transformations within the film crystal lattice structure [5].

Residual stress is defined as stress that is inherent within a material due to the forces present between the film and the substrate it is deposited on and between individual lamina within a multilayer material. If the thin film were removed from the substrate, this stress also would be minimized or removed if such orientation is possible [6].
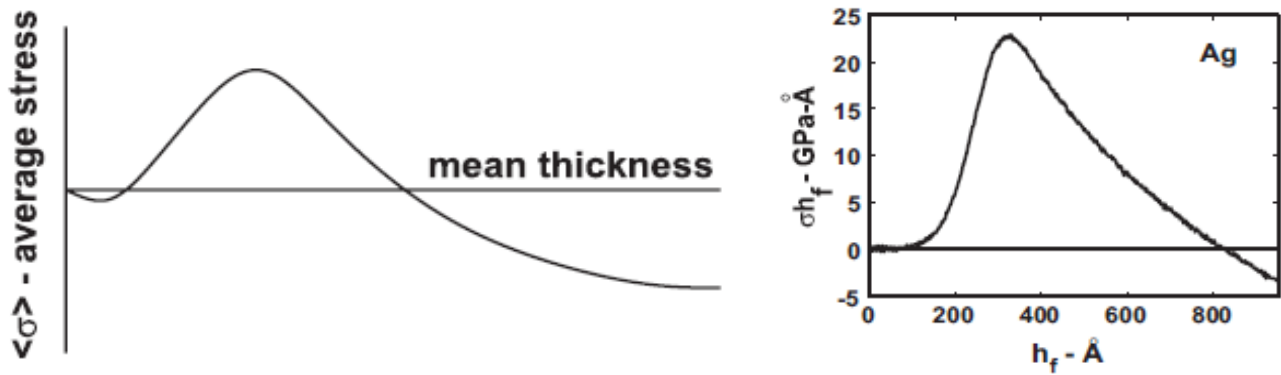
Figure 1: Average film stress vs. mean film thickness. In both plots, negative average stress represent compressive stress within the film and positive average stresses represent tensile stress. A general trend of films developing first with compressive stress, then tensile stress, and finally compressive stress can be seen in a wide range of thin film materials. The average film stress x mean film thickness vs mean film thickness for deposition of silver is shown in the plot on the right. Figure take from Ref. [7].

As a film is deposited, a common trend in the volume-average film stress verses film thickness is observed. This relationship shown in Figure 1 (left) is common in a wide range of film materials. The plot in Figure 1 (right) shows the relationship between the product of stress and film thickness verse film thickness. Note that silver follows the general trend of the film experiencing a progression from compressive forces at small thicknesses, then tensile forces, and eventually compressive forces again as the thickness increases. Plots such as these are created by measuring the curvature of thin films as they are being deposited at constant rates. In this method, the curvature is measured as a function of time. The deposition rate can be used to calculate the thickness and the curvature can be used to calculate the average stress in the film-substrate system as described in Section 2.3.

1.1.3   Driving Forces

The research group of Baker, Hoffman, Timian, Silvernail, and Ellis published their findings displaying a lack of understanding regarding the behavior of thin silver films. The face centered cubic crystal structure of silver, shown in Figure 2, is deposited predominantly in one orientation and upon transforms when annealed. The transformation observed during the annealing process has been theorized to be a result of strain and interface energy minimization. In the data examined by the group, stresses in the samples were less than what the current theory would expect to be required to initiate the texture transformation. Despite the lack of sufficient stress, transformation still occurred. In other experiments the driving forces were examined further by placing titanium and nitride interfaces between the substrate and film, each resulting in different interface and stress energies. Results showed transformations occurring at approximately the same thickness independent of the interface material present. In addition, the driving force increased with film thickness, suggesting a different driving force, possibly a reduction of defect energy [8]. The lack of a satisfactory theory that uses physical driving forces to predict the observed transformations requires more research.
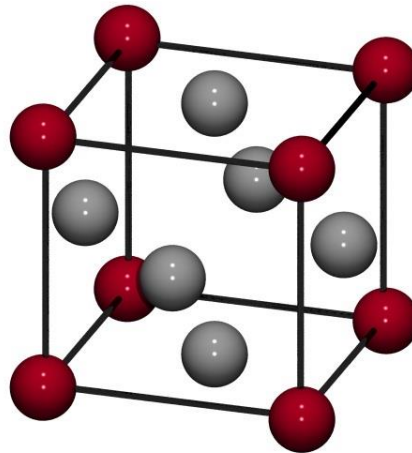

Figure 2: The crystal structure of silver, face centered cubic. When deposited, silver is primarily oriented such that the cube stands on one corner. As the film is annealed, a transformation occurs to an orientation where the cube lies on a face.

1.2   Interference of Light

In 1802, Thomas Young theorized that light undulations [waves] when combined produce waves of greater intensity or less intensity based on the motion of the undulation at the intersection point. Later, he published an experiment using a beam of sunlight and a narrow card to display light interference patterns. The light beam would pass on either side of the card but not through the card so patterns of interference were observed on a screen behind the card at various distances. From this experiment Young noted uniform spacing of light fringes, explainable by interference of light from either side of the card [10] as shown in Figure 3.
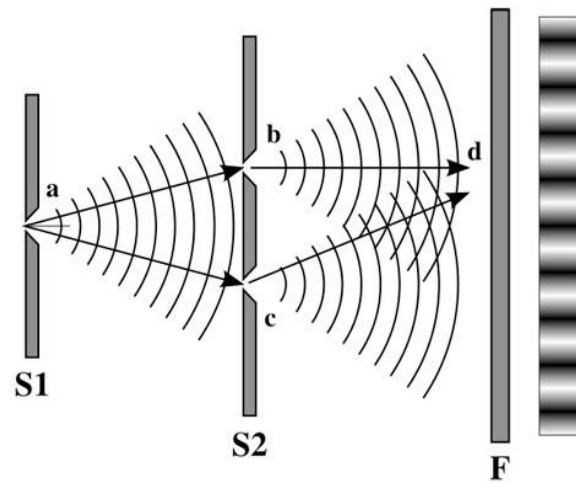
Figure 3: Wave interference of light through double slit. The light originates at point (a) and travels toward S2 at which it passes through the holes located at (b) and (c). The light then travels toward F. The light and dark bands produced by the interference of the two waves is shown at the far left. The distance the light traveled from (b) to (d) and from (c) to (d) relative to each other determines if a light or dark band is produced at (d). Figure taken from Ref. [11].

1.3   Interferometer History

1.3.1   Interferometer Introduction

Light interference is the principle concept upon which interferometers are built and results are interpreted. The combined waves form an image, often displayed on a screen which can then be analyzed.

1.3.2   *Michaelson-Morley Interferometer*

Albert Michaelson and Edward Morley were the first two experimentalists to develop and use an interferometer. In 1887 they attempted to detect the speed of luminiferous ether relative to the motion of earth [12].
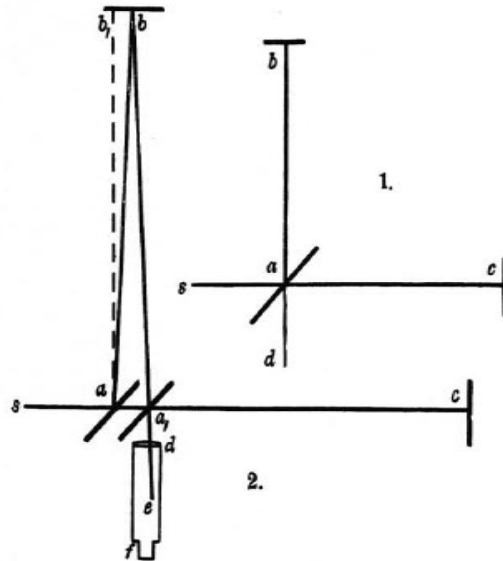
Figure 4: Original Michaelson-Morley interferometer apparatus. Diagram 1 is a schematic Diagram of the original Michaelson-Morley interferometer apparatus and Diagram 2 is what was expected as a result of relative motion in a luminiferous ether. This is the first use of an interferometer. Figure taken from Ref. [12].

In Figure 4 Diagram 1, the light beam enters from the left from and is split at a half silvered mirror (a) which allows part of the light to be reflected toward (b) and part of the light to pass through toward (c). From there, two beams a light travel along the shown path, reflect off their respective mirrors at (b) and (c) and return to the beam splitter at (a). Lastly the light is reflected off the beam splitter and travels toward (d) where a detector or screen is present. In Diagram 2 of Figure 4, the dotted line from (a) to b_1 depicts the overlap of Diagram 1. As light passed through ether, the path difference due to the rotation of the earth was expected to change. Then by geometry, the distance traveled could be calculated with respect to the other path and the velocity of ether relative to the earth could be measured.

1.3.3   Twyman-Green Interferometer

The Twyman-Green interferometer is similar to the Michaelson-Morley interferometer with the addition of diverging and collimating lenses and a uniform light source. A diverging lens would broaden the beam of light and a collimating lens would produce parallel rays of light such that, when they were reflected off their respective mirrors, the reflected light would pass back through the same lens and be focused back toward the half silvered mirror [13]. The combined light would then be projected on a screen. A Twyman-Green interferometer is shown in Figure 5 with the addition of piezo electric ceramic actuator controlling a mirror, which was not a feature of the original design. Additionally, a Cooper-Hewitt mercury vapor lamp was used to produce a light source that consisted of few homogeneous wavelengths rather than a spectrum of wavelengths achieved from sunlight [14]. These new additions allowed for the examination of large surfaces (often the surface of lens elements) from observations of the light interference pattern on a screen. The intention of the interferometer apparatus was for commercial testing of camera lenses [15].

1.3.4   Phase-Stepping Interferometry

Measuring elements to within fractions of a fringe distance while reducing noise can be done with the use of a phase-stepping interferometer. First developed by Bruning, Herriott, Gallagher, Rosenfeld, White, and Brangaccio in 1974, the phase-stepping interferometer employed new features to accomplish higher resolution images. The implementation of a piezoelectrically controlled mirror was added to examine the image with varied path lengths which allows for the measurement of elements to within fractions of a fringe distance. The mirror would move parallel to the incident beam, changing the total path length of the reference beam. The apparatus light source was converted from a mercury vapor lamp to a frequency stabilized single frequency laser to greater improve the reproducibility and accuracy of the final contour image [16].

In a paper published by Lee, Tien, and Hsu in 2002, the research group investigated the internal stress properties of Nb_2O_5 thin films, deposited by the method of ion-beam-sputtering-deposition, with an interferometer. An optical monitor was used to determine the film's thickness. Additionally, a quartz-crystal monitor was employed to measure the deposition rate which could be used to verify the

thickness measurement of the optical monitor. The team used a phase-shifting Twyman-Green interferometer with a laser wavelength of 650 nm. The interferometer apparatus was used to measure the curvature of the film. Stoney's formula was applied to the curvature measurements to calculate the stress in the thin film [17].

A multiple-wavelength technique was incorporated into the phase-stepping interferometer constructed by Lewis to measure the length of metal bars with increased length accuracy. The final uncertainty achieved with the interferometer was $\pm68\pm350L$ nm where L is the length of the bar in meters. In the system, three different light sources with different wavelengths, 633 nm, 612 nm, and 543 nm were used. A topographical map can be made with a single wavelength light source however the accuracy of the measurement is limited by the ability to measure the length of the bar to within $\pm$ ¼ fringes. This limitation can be overcome by adding a second light source of similar wavelength. The addition produces a pattern in which the two individual patterns combine to form regions where bright fringes form due to the combination of the two patterns allowing for the length of the bar to be measured to within ±9 μm. Further accuracy is gained with the addition of a third light source with wavelength similar to that of the first two light sources. Lewis' apparatus was able to take a measurement in under two minutes and produce length, flatness, and parallelism measurements, an improvement on previous machines that took longer and had higher uncertainties [18].
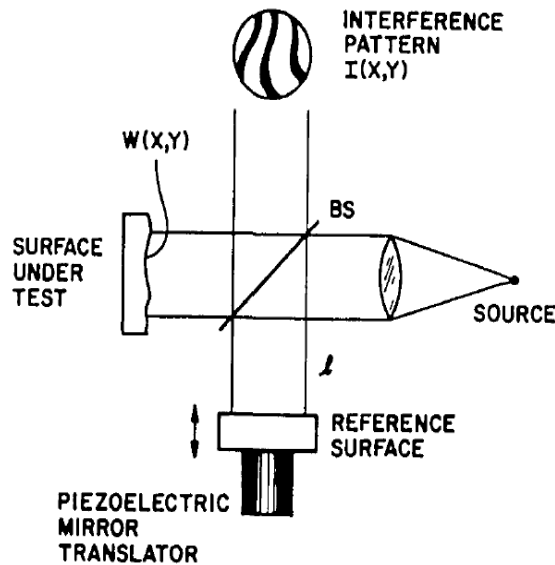
Figure 5: Phase-Stepping Twyman-Green interferometer. This shows a schematic diagram of a phase-stepping interferometer with a piezoelectric controlled reference mirror. The laser produces light which is collimated by a lens and then contacts the beam splitter denoted by 'BS'. The light reflects off the reference surface and the surface under test respectively. The reflected beams are combined at BS and are displayed as in interference pattern where I(X,Y) is intensity as a function of position. Figure taken from Ref. [16].

1.4   The Houghton Interferometer

A phase-stepping interferometer is being constructed at Houghton College to measure the thin films formed by the method of vapor deposition in the Houghton College Deposition Chamber [19]. The system uses a computer controlled piezoelectric reference mirror to vary the phase on the reference beam. The recombined beam is displayed on a screen and images are taken at constant time intervals by a webcam. Lastly, the images are processed by a computer program to produce a contour map of the surface of the film. Gradients as large as one-quarter wavelength variations per pixel can be measured, allowing for our apparatus to measure a constant gradient change with a total thickness change of up to 150μm.

The purpose of constructing a laser interferometer is to use the interference wave property of light to construct in-situ topographical images of thin metal films. The thin films are formed in a deposition

13

chamber under vacuum. Measuring the film while still under vacuum allows for limited contamination that could result from exposure to air and particulates outside vacuum. These images can then be used to measure curvature and, by extension, predict stress within the thin metal film. Alternatively, if a film is stepped, that is deposited in such a way as to produce a stepped thickness gradient, the interferometer will identify regions in which thickness changes occur.

The system will be mounted under the deposition chamber with the sample beam reflecting off the thin film inside the deposition chamber. The chamber-interferometer apparatus will be suspended from large springs to lessen building vibrations resulting in limited image disturbance. Additionally, the interferometer will be mounted using threaded rod such that the interferometer can be adjusted to provide a path for the beam to reflect off the in-situ substrate and return unobstructed.

The interferometer is composed of several lenses and mirrors that are imperfect, thus they themselves will produce an interference pattern. Additionally, before deposition occurs, the substrate is likely to be curved or have minor imperfections resulting in additional interference patterns. Only the interference pattern due to the deposition of metal is desired. Thus, the interferometer will take a picture of the substrate before deposition as a reference picture and take pictures after deposition. This will allow the determination of the topography of the thin film regardless of the topography of the initial substrate. Quick and consistent topographical images of thin films in-situ are the motivation for constructing an interferometer at Houghton College.

Chapter 2

THEORY

2.1   Waves

2.1.1   Waves Introduction

Light is an electromagnetic wave that is composed of orthogonal electric and magnetic fields. Both the electric and magnetic fields are sinusoidal waves that can be written in terms of the maximum magnitude of the electric and magnetic fields, the angular wave number, and the angular frequency, as a function of time and position. Light exhibits the characteristics of waves in some situations and particles in others, a phenomenon commonly referred to as wave-particle duality.

The general expression for a sinusoidal wave is

$$E(x,t) = A\sin(kx - \omega t + \varphi) \tag{1}$$

where $E(x,t)$ is the electric field of the light wave at position x and time t. The wave phase shift is φ. A is the amplitude of the wave. The angular frequency, ω, is defined as

$$\omega \equiv 2\pi f \tag{2}$$

where f is the frequency of the wave. The wave number, k, is defined as

$$k \equiv \frac{2\pi}{\lambda} \tag{3}$$

where λ is the wavelength.

2.1.2   Interference

In an interferometer, the reflected light beams are combined. The combined beam is then reflected toward the screen for imaging. In the recombination process, interference occurs and results in an

interference pattern as the two beams overlap. If one on the beams were to be covered, no interference pattern would result because interference requires the presence of both beams simultaneously.
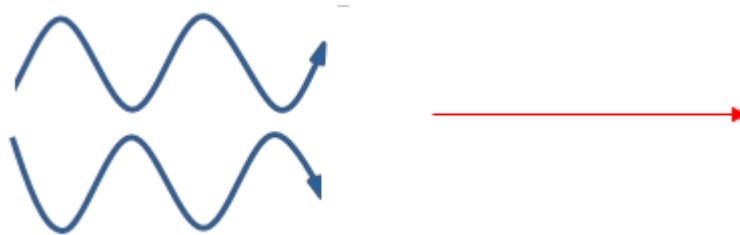

Figure 6: Destructive Interference. Two incident waves (blue) result in a net amplitude of zero because they are 180 degrees out of phase from each other. They combine to from the red wave.
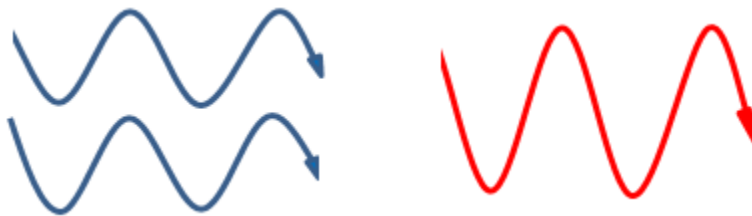
Figure 7: Constructive Interference. Two incident waves (blue) result in a net amplitude of double the original amplitude because they are in phase with respect to each other. They combine to from the red wave with the same frequency but double the amplitude of the blue waves.

As seen in Figure 6, the combination of the two incident waves (blue) would result in a wave of amplitude zero (red) because the waves are opposite each other, also referred to as 180° out of phase. This would be seen as the absence of light, or a dark spot on the screen of an interferometer. In Figure 7, both incident waves (blue) have the same phase. Thus, when they combine they will construct a wave with double the amplitude of the incident waves. A more general function for the amplitude of two combined waves can be derived by considering the sum of two sinusoids that have some arbitrary phase:

$$E(x,t) = E_1(x,t) + E_2(x,t) \tag{4}$$

$$E(x,t) = A\sin(kx - \omega t + \varphi_1) + A\sin(kx - \omega t + \varphi_2) \tag{5}$$

The two incident waves originate from the same source, a monochromatic laser, thus they have the same amplitude and frequency, differing only by the phase.

Application of the trig identity,

$$\sin\alpha \pm \sin\beta = 2\sin\left[\frac{1}{2}(\alpha \pm \beta)\right]\cos\left[\frac{1}{2}(\alpha \mp \beta)\right], \tag{6}$$

to Eq. 6 produces

$$E = 2A\cos\left(\frac{\varphi_1 - \varphi_2}{2}\right)\sin\left(kx - \omega t + \frac{\varphi_1 - \varphi_2}{2}\right). \tag{7}$$

The intensity of a wave, I, is written as,

$$I \propto E^2 \tag{8}$$

which can be written as

$$I \propto 4A^2\cos^2\left(\frac{\varphi_1 - \varphi_2}{2}\right)\sin^2\left(kx - \omega t + \frac{\varphi_1 - \varphi_2}{2}\right) \tag{9}$$

by substituting Eq. 8 into Eq. 7.

The average intensity, I_{avg}, is what is actually observed from the combined beam. It is defined as

$$I_{avg} \propto \frac{\left\{2A\cos\left(\frac{\varphi_1 - \varphi_2}{2}\right)\right\}^2}{2} \equiv \frac{(A')^2}{2} \tag{10}$$

where A' is the amplitude of the combined intensity wave as shown in Eq. 9. Thus,

$$I_{avg} = B cos^2 \left(\frac{\varphi_1 - \varphi_2}{2} \right) \tag{11}$$

where B is a proportionality constant. We can see that the average intensity of the combined beam is proportional to the cosine squared of the difference in phase shift of the two incident beams.

The difference in phase between two incident waves can be written as

$$(\varphi_1 - \varphi_2) = \frac{2\pi}{\lambda} (L_1 - L_2) = \frac{2\pi}{\lambda} \Delta L \tag{12}$$

where

$$\Delta L \equiv L_1 - L_2. \tag{13}$$

Physically, L_1 is the path length of the incident beam from the beam splitter to a point on the reference mirror and back. L_2 is the path length of the incident beam from the beam splitter to a point on the sample mirror and back. The distance that is necessary for analysis is not the total path length of the beams but the difference in path length of the beams, ΔL. For our system, we will be analyzing images of the combined beam, which is the beam produced from the combination of the two incident beams that return following the reflection off the sample and reference mirrors respectively. The images are composed of individual pixels, thus the points discussed will be pixels.

Substituting Eq. 13 into Eq.11 yields

$$I_{avg} = cos^2 \left[\frac{2\pi}{\lambda} (\Delta L) \right]. \tag{14}$$

Eq. 14 shows the relationship between the average intensity of the combined beam and the difference in the path lengths of the two incident beams. We can further write

$$I_{avg} = \cos^2\left[\frac{2\pi}{\lambda}(\Delta L_0 + x)\right] \tag{15}$$

where

$$\Delta L = \Delta L_0 + x \tag{16}$$

where x is the position of the reference mirror and ΔL_0 is the path length difference for that pixel when $x = 0$. This is done because as the reference mirror moves, x changes while ΔL_0 remains constant.

2.2   Sine-Squared Function

Examination of one small portion of the beam cross-section of the combined beam will result in an Intensity vs. x function as the path length difference changes. A different small portion of the cross-section of the combined beam will have a similar Intensity vs. x function but may be shifted slightly due to a difference in overall path length of the component beams, resulting in different ΔL_0 values. This would be expected if the mirrors were not perfectly flat. When the two functions from are plotted on the same graph, a function shift, ψ, can be seen as shown in Figure 8. In this example, the function shown in red has a different ΔL_0 value than that of the function shown in blue. The difference in the ΔL_0 values are shown in Figure 8 as a different variable, ψ, for clarity.

With an interferometer, a comparison of the function shifts of adjacent portions of the beam cross-sections will be used to form a topographical image of a film surface. This topographical image will then be used to determine the stress within the film based on the curvature of the film.
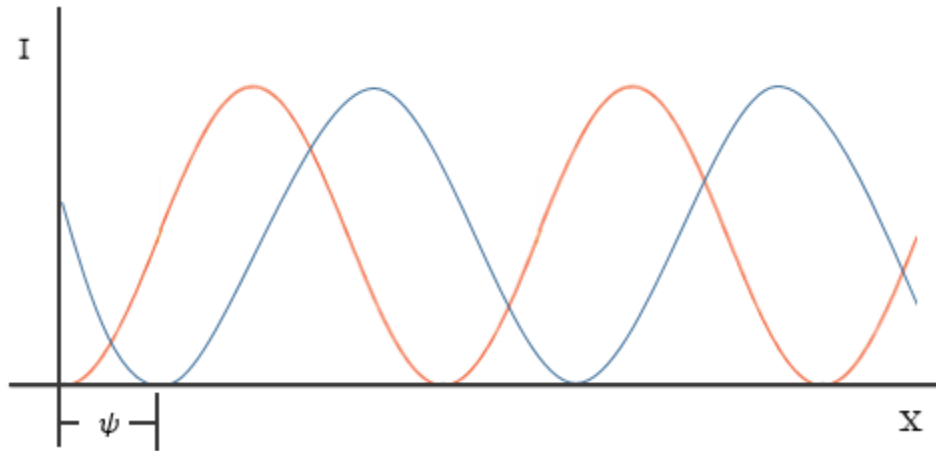
Figure 8: Two Sine Squared functions of Intensity vs. x. The difference in phase between the red and blue functions is the phase shift between the two adjacent cross-sections of the combined beam.

2.3 Stoney Formula

The Stoney Formula describes a relationship between the stress within a thin film and the resulting curvature of the film [20]. This is also dependent upon the material and thicknesses of the film and the substrate.

Figure 9: A film-substrate system. Moments and forces within the system are shown. M_s and M_f are the bending moments of the substrate and film respectively. F_s and F_f are the forces at the interface of the substrate and film respectively.

20

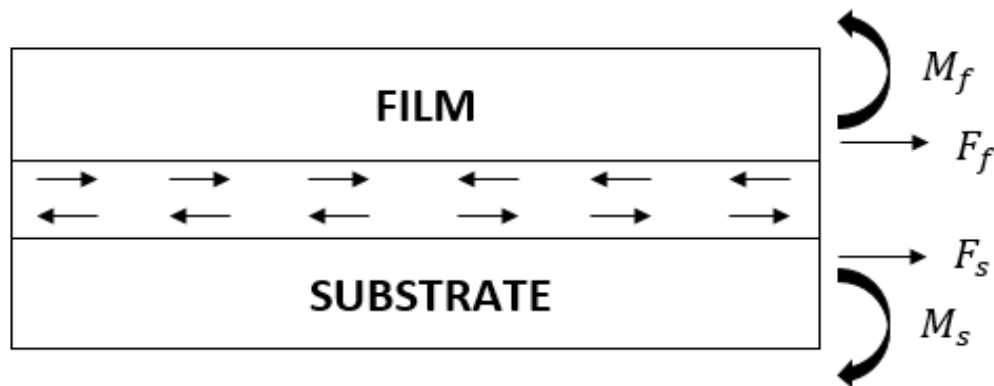The forces, F_f and F_s, must be equal. Thus, we get the equation,

$$F_f = F_s \equiv F \tag{17}$$

where F_f is the force acting on the film due to the substrate, and F_s is the force acting on the substrate due to the film. The forces are assumed to act uniformly over the cross-sectional area of the interface, A, which can be written as

$$A = d_f w \tag{18}$$

where d_f is the thickness of the film and w is the width of the film.

The sum of the moments on the substrate shown in Figure 9 are equal to zero, thus the moment on the substrate due to the film, M_f, and the moment on the substrate due to internal stress, M_s, must be equal.

$$\Sigma M_{substrate} = 0 = M_f + M_s \tag{19}$$

Stress, σ, is defined as the force per unit area. The maximum stress from tension or compression at the outer edges is $+\sigma_m$ and $-\sigma_m$ respectively and

$$\sigma_m = Y\epsilon \tag{20}$$

where Y is the Young's modulus and ϵ is the strain, defined as

$$\epsilon = \frac{\Delta L}{L} \tag{21}$$

where L is the length of the system shown in Figure 10.
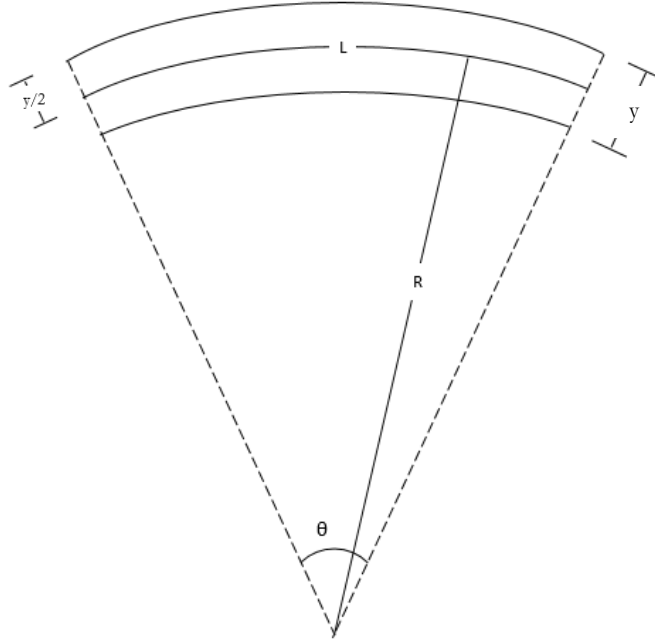
Figure 10: A curved Substrate-Film System. The system has total thickness, y, and a radius of curvature, R. The length, L, is the length of the system with no curvature.

Thus,

$$\epsilon = \frac{\Delta L}{L} = \frac{\left(R \pm \frac{y}{2}\right)\theta - R\theta}{R\theta}. \tag{22}$$

Substituting ϵ from Eq. 22 into Eq. 20 yields

$$\sigma_m = Y\left\{\frac{\left(R \pm \frac{d}{2}\right)\theta - R\theta}{R\theta}\right\} = \pm\frac{Yd}{2R}. \tag{23}$$

Using the stress distribution, the bending moment for the beam section is

$$M = \int_{\frac{-y}{2}}^{\frac{y}{2}} \sigma_m wy \, dy \qquad (24)$$

Substitution of Eq. 23 into Eq. 24 results yields

$$M = \frac{Yw}{2R} \int_{\frac{-y}{2}}^{\frac{y}{2}} y^2 \, dy \qquad (25)$$

Integration of Eq. 24 over the thickness of the system results in

$$M = \frac{Yd^3 w}{12R}. \qquad (26)$$

The moment depicted in Figure 10 is that of the moment on the substrate due to internal stress, thus,

$$M_s = \frac{Y_s d_s^{\,3} w}{12R}. \qquad (27)$$

Currently we are considering a 1-D system where stress, σ, and strain, ϵ, can be related by Hooke's Law:

$$\epsilon = \frac{\sigma}{Y}. \qquad (28)$$

Consider a 2-D system with stress in the x and y directions and zero stress in the z direction. A stress in the x direction, σ_x, will produce a strain in the x direction, ϵ_x, similar to Eq. 28 where

$$\epsilon_x = \frac{\sigma_x}{Y}. \qquad (29)$$

The stress in the y direction will result in a strain in the y direction and to preserve volume, will produce a strain in the x direction. The magnitude of the strain produced in the x direction as a result of the

stress in the y direction is related by Poisson's ratio, ν. Thus, the total strain in the x direction due to the stress in the x and y directions is

$$\epsilon_x = \frac{(\sigma_x - \nu\sigma_y)}{Y}. \tag{30}$$

If $\sigma_x = \sigma_y$, then

$$\epsilon_x = \frac{(\sigma_x - \nu\sigma_x)}{Y} = \frac{(1-\nu)}{Y}\sigma_x = \frac{\sigma_x}{B} \tag{31}$$

where B is the biaxial modulus. Thus,

$$B = \frac{Y}{(1-\nu)}. \tag{32}$$

Therefore to account for a biaxial stress distribution rather than a uniaxial stress distribution in Eq. 27, we must replace Y_s with $\frac{Y_s}{1-\nu_s}$. This yields

$$M_s = \frac{Y_s d_s{}^3 w}{12R(1-\nu_s)} \tag{33}$$

Stress due to the film is defined as

$$\sigma_f \equiv \frac{F}{A} = \frac{F_f}{d_f w}. \tag{34}$$

The moment on the substrate due to the film is

$$M_f = F_f \left(\frac{d_s}{2}\right). \tag{35}$$

Substituting Eq. 34 into Eq. 35 results in

$$M_f = \sigma_f d_f w \left(\frac{d_s}{2}\right). \tag{36}$$

Substituting M_s from Eq. 33 and M_f from Eq. 36 into Eq. 19 produces

$$\sigma_{f=} \frac{Y_s d_s^{\,2}}{6R(1 - v_f)d_f}. \tag{37}$$

The radius of curvature, R can be written in terms of κ by

$$\kappa = \frac{1}{R}. \tag{38}$$

Finally, substitution of κ results in the Stoney Formula,

$$\sigma_{f=} \frac{\kappa Y_s d_s^{\,2}}{6(1 - v_f)d_f}. \tag{39}$$

Examination of Eq. 39 shows a direct proportionality of the stress within the film and the curvature. With all other constants known, the curvature of the film found using a phase stepping interferometer can be used to calculate the stress within the thin film.

EXPERIMENTAL/APPARATUS

3.1   Experimental Apparatus

3.1.1   Introduction

The laser interferometer is constructed upon a 24 in x 36 in optics table shown in Figure 11. The optics table is currently resting on top of a pneumatic floating table to reduce vibrations that can cause image instability.
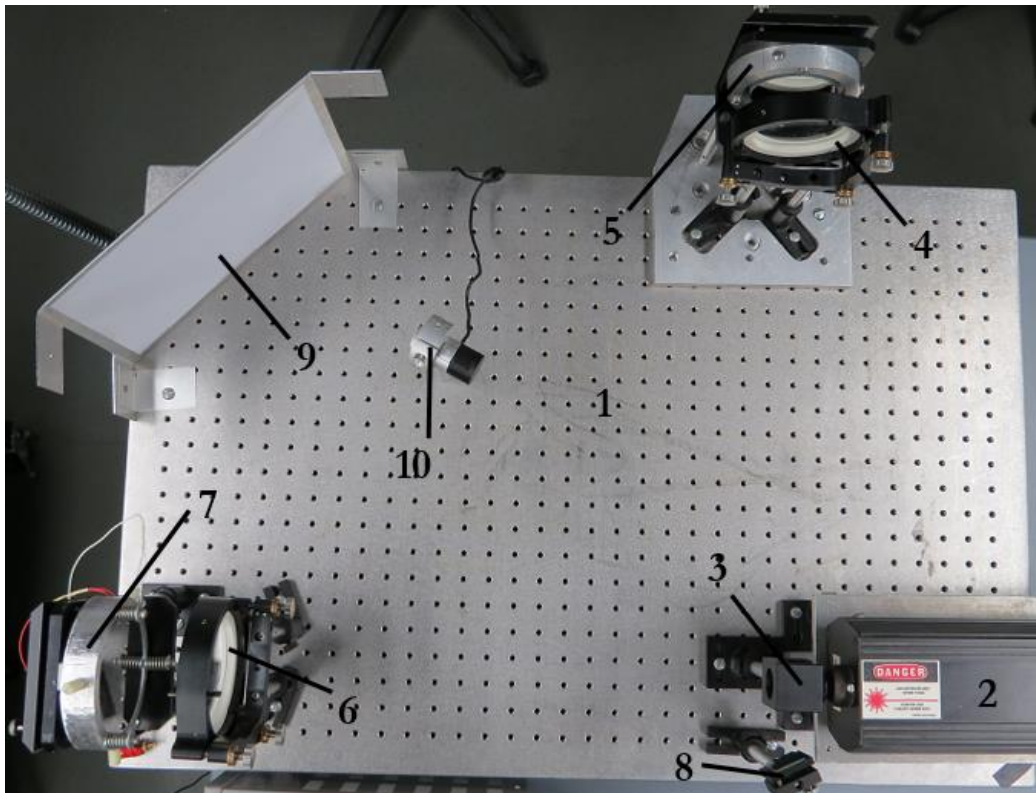

Figure 11: Image of Experimental Apparatus. 1: Optics Table. 2: 632nm Laser. 3: Diverging lens and Beam Splitter. 4: Sample Collimating Lens. 5: Sample Mirror. 6: Reference Collimating Lens. 7: Reference Mirror. 8: Image Redirection Mirror. 9: Screen. 10: webcam.
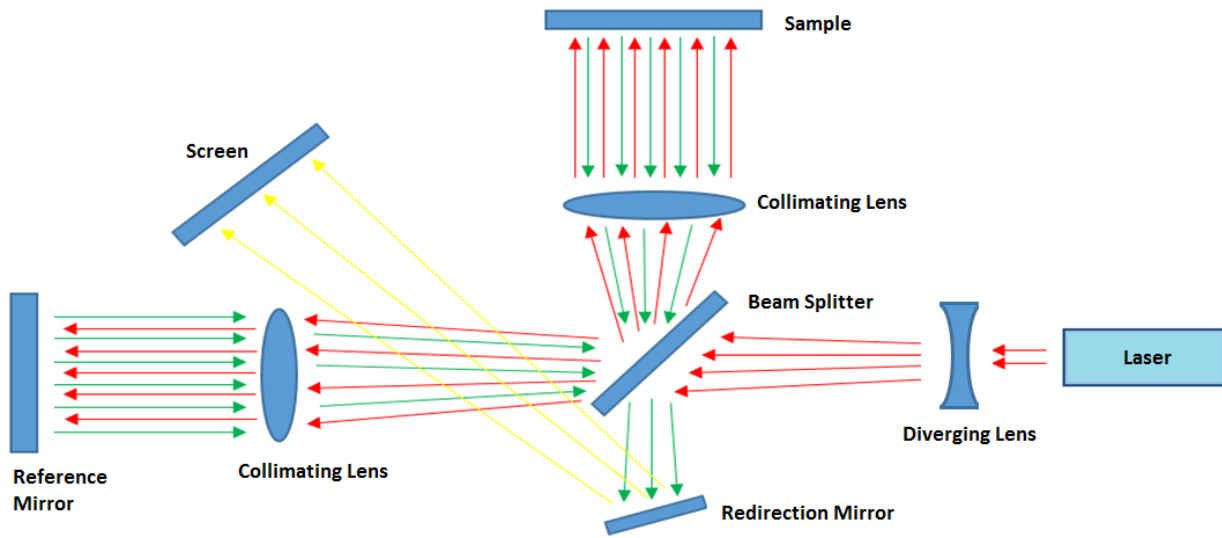
Figure 12: Block diagram of experimental apparatus with beam path shown. The red arrows represent the beam traveling to the beam splitter and the split beam traveling to the reference mirror and the sample respectively. The green arrows represent the beam path as the light returns to the beam splitter from the reference mirror and the sample. The yellow arrows represent the recombined beam traveling to the screen, where the interference patter in seen and photographed.

The path of the laser beam is shown in Figure 12. The laser beam passes through the diverging lens and is split into two beams by the beam splitter. The two beams are collimated by their respective converging lens and travel toward their respective mirror. The beams then reflect off their mirrors and pass through the corresponding collimating lens again. The two beams recombine into one beam at the beam splitter. This combined beam then reflects off the image redirection mirror and finally produces an interference pattern on the screen. A webcam shown in Figure 11 takes pictures of the interference for processing.

3.1.2 Laser/ Beam Splitter

An Aerotech LS5R, 15 mW, 632 nm laser is used to provide a monochromatic light beam. The laser beam initially passes through a diverging lens that is attached directly to the beam splitter encasing as shown in Figure 13. The diverging lens allows the collimated laser beam to diverge to a diameter of 3.25 inches when it reaches the reference and sample collimating lenses. The beam splitter is composed of a

half silvered mirror which allows half of the light to pass through while half is reflected. The half-silvered mirror is angled at 45° relative to the incident beam which results in the reflected light beam traveling perpendicular to the beam incident on the mirror. The beam splitter is used again as the light beams return from their respective mirrors allowing for the combination of the two separate beams into one beam.

In Figure 14, the reflected beams (represented as blue and yellow) return from their respective mirrors and contact the half-silvered mirror, where each are split in the same fashion as the original beam in Figure 14. The beam returning from the sample mirror contacts the half silvered mirror and is split with half passing through and half being reflected toward the laser. The beam returning from the reference mirror contacts the half silvered mirror and is split with half passing through toward the laser and half being reflected. The recombined beams shown in green will travel toward the laser and the image redirection mirror. The combined beam that travels toward the laser is not used while the recombined beam shown traveling down in Figure 14 will be reflected off a redirection mirror and produce an interference pattern on a screen. This will be photographed using a webcam.
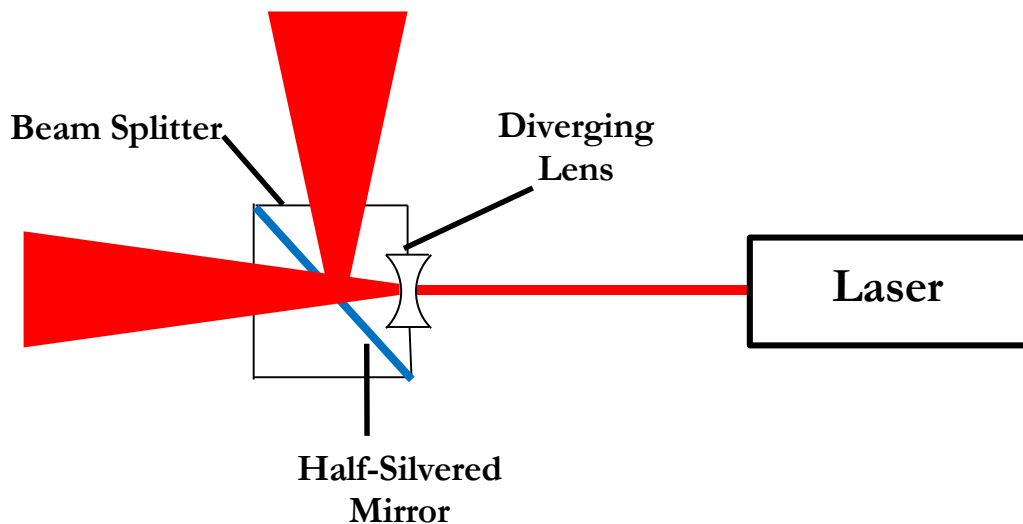

Figure 13: Laser, diverging lens and beam splitter apparatus with beam path. The collimated laser passes through the diverging lens and contacts the beam splitter's half-silvered mirror. Half of the light passes through the mirror and half is reflected.
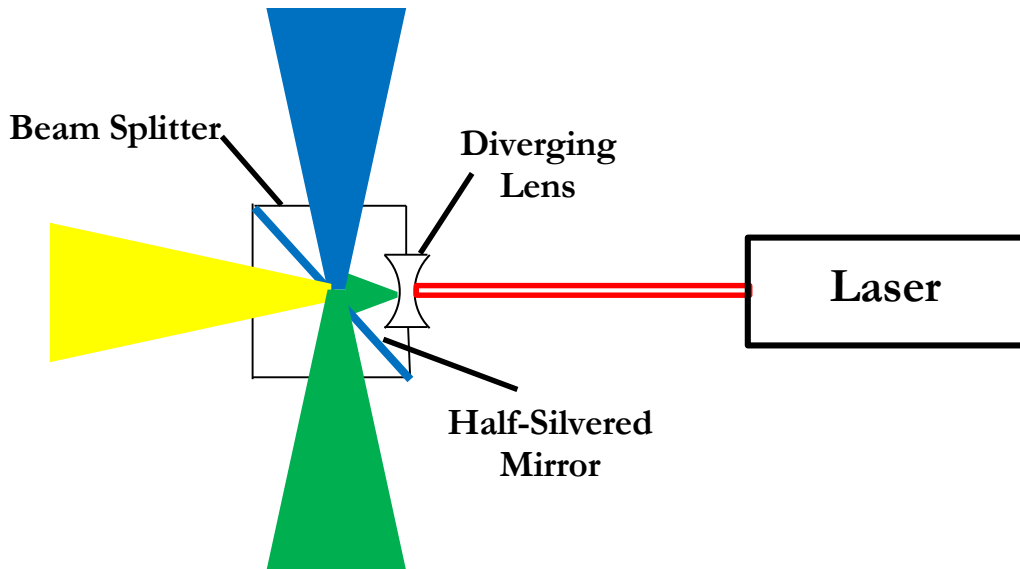
Figure 14: Beam Splitter with beam path during beam recombination. The reflected beam from the sample mirror (blue) and the reflected beam from the reference mirror (yellow) contact the beam splitter. Combined beams (green) travel toward the laser and the redirection mirror.

3.1.3   Collimating Lenses

Two converging lenses with focal lengths of 6mm are used, one for each beam, to focus a diverging beam into a 3.25 inch diameter collimated beam. Each beam will then contact its respective mirror and reflect back through the collimating lenses. The lenses will focus their respective beam, resulting in the beams traveling to the beam splitter along their original paths.

3.1.4   Reference Mirror

The reference mirror is composed of a 4 in diameter, $\frac{1}{10}\lambda$ optically flat mirror, an aluminum mirror mount, three piezoelectric ceramic actuators, three springs, and an adjustable kinematic mount as shown in Figure 15.
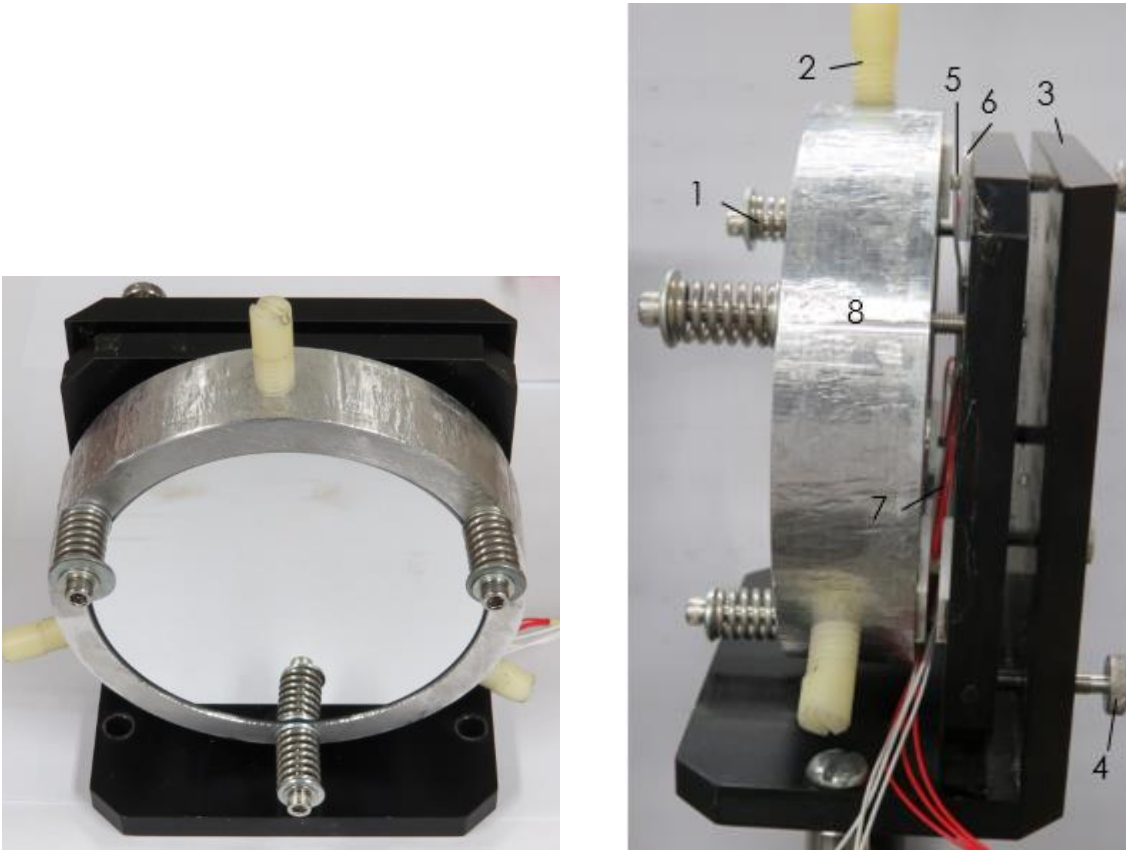
Figure 15: Front and side view of reference mirror. The front view of the reference mirror (left) shows the 4 inch reference mirror. The side view (right) shows: 1: Compression springs, 2: Plastic set screws, 3: Kinematic Mount, 4: Mount adjustment screws, 5: Piezoelectric ceramic actuator, 6: ceramic buffers, 7: Piezoelectric ceramic actuator leads, 8: Mirror holder. The reference mirror's motion is a result of the piezoelectric ceramic actuators and results in a changing interference pattern.

The piezoelectric ceramic actuators implemented will expand and contract as a potential difference of 0-60 V is placed across the actuator. They will move the reference mirror parallel to the incident beam. The LabVIEW program controlling the piezoelectric actuators will output a voltage changing at a constant rate, thus the reference mirror will move at a constant rate. The 0-60 V potential difference across the piezoelectric ceramic actuators will result in a total displacement of approximately 850 nm. The piezoelectric ceramic actuators are mounted behind the mirror holder, situated between two pieces

of ceramic. This keeps the leads from contacting the aluminum sample holder and mirror mount. The three positive leads are soldered together and the three negative leads are soldered together to produce a circuit where all three piezoelectric ceramic actuators are in parallel. This ensures an equal potential across each actuator, resulting in even mirror displacement.

Three plastic screws are used to hold the mirror in place while reducing the possibility of fracturing the mirror from overtightening. In addition, three screws are used to fasten the mirror mount to the adjustable sample holder, each compressing a spring with spring rate of 38.1 lbf/in. This is required because piezoelectric ceramic actuators are required to be under compression to operate.

3.1.5   Sample Mirror

A 3 inch diameter $\frac{1}{10}\lambda$ optically flat mirror is implemented in the interferometer to take the place of an actual sample for testing purposes. Currently the sample mirror is fastened much like the reference mirror in that it is held in the mount by three screws each with a plastic tip to protect from overtightening induced fracture. The sample mirror, unlike the reference mirror, is stationary. Once the testing phase of the instrument is complete, and the interferometer is operational, the sample mirror will be replaced with a thin film for analysis.

3.1.6   Screen/ Webcam

The recombined image from the beam splitter is reflected off the image redirection mirror and onto the screen. A 1 megapixel webcam controlled by a computer program, YAWCAM, captures the interference pattern that is displayed on the screen. As the reference mirror moves, the webcam takes photographs of the screen at constant intervals. The pictures are numbered and saved in a folder to be analyzed by a LabVIEW program.

3.2   DAQ/Op-Amp Circuit

3.2.1   Introduction

A National Instruments DAQ (NI USB-6008) is implemented because the device is an interface that can output and input current or voltage signals with a LabVIEW program. The DAQ, because it is

interfaced via USB, has a voltage limitation of 0-5 V. The interferometer reference mirror is driven by a voltage potential across the piezoelectric ceramic actuators of 0-60 V. The DAQ voltage output limitation requires the use of an amplification circuit; an Op-Amp circuit is used.

3.2.2   Op-Amp Circuit
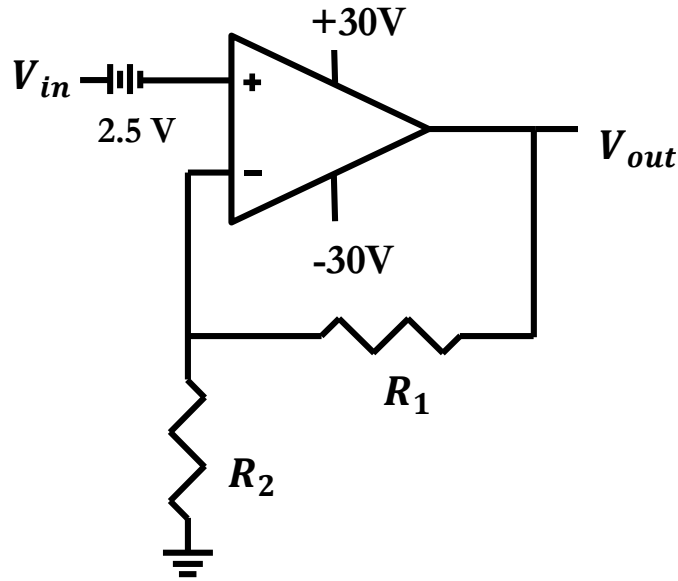

Figure 16: Circuit Diagram of Op-Amp Circuit. The Op-Amp circuit is a non-inverting amplifier with amplification of 12.1. $R_1 = 100\ M\Omega$ and $R_2 = 9\ M\Omega$. The 2.5 V power supply decreases the voltage input into the positive input of the Op-Amp resulting in an output of -30 V to 30 V.

The signal from the DAQ output is input into a constant voltage power supply of 2.5 V to produce V_{in} voltage ranges from -2.5 V to 2.5 V. Analyzing the Op-Amp circuit shown in Figure 16 produces a linear relationship of

$$V_{out} = (V_{in} - 2.5\ V)\left(\frac{R_1 + R_2}{R_2}\right) \tag{40}$$

32

$$V_{out} = 12.1 \, (V_{in} - 2.5 \, V).\tag{41}$$

Thus, the output voltage is roughly -30V to 30V. One lead of the piezoelectric ceramic actuators is connected to -30V while the other lead varies from -30V to 30V resulting in a total potential difference of roughly 0V to 60V.

3.3 LabVIEW Program

3.3.1 Introduction

A LabVIEW program has been written to automatically create a set of interference images by controlling a webcam to photograph the screen as shown in Figure 11. The program analyzes the images by examining each individual pixel relative to the neighboring pixel to develop a topographical image of the sample.

3.3.2 Image Set Creation

As the LabVIEW program runs, it will output a voltage via the National Instruments DAQ to the amplifying circuit which will drive the piezoelectric ceramics and move the reference mirror. As the mirror moves, the path length of the reference beam will change, resulting in a different interference pattern when the reference beam and sample beams combine. The webcam will take pictures regularly, with a frequency determined by the user, and save the pictures with a name indicating the order in which they were taken. The group of images are all saved in the same folder and are considered a set of interference images.

3.3.3 *Pixel Analysis*

The LabVIEW program imports a set of images and creates a three-dimensional intensity array. As shown in Figure 17, the array is composed of the images in the set stacked on each other. The light intensity of each pixel is determined by the program.
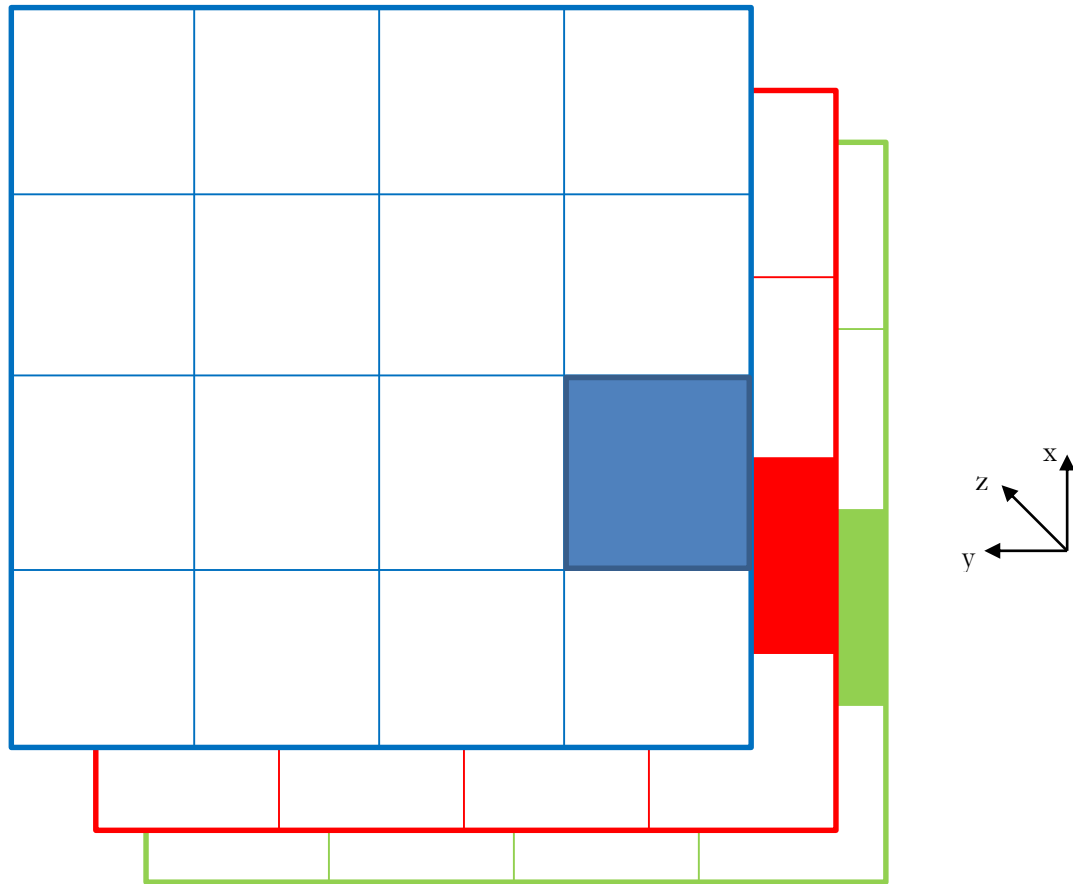
Figure 17: A simple three-dimensional array composed of three images. The three images are represented as three colors: blue, red, and green. In the x-y plane are the images; each square represents a pixel. The images are stacked on top of one another in the z-direction resulting in a three dimensional array. The shaded square on each represents a single pixel.

The three-dimensional array shown in Figure 17 is composed of three images shown as three colors: green, red, and blue; each image is four pixels by four pixels. The three images form a three-dimensional

array (4x4x3) that is composed of two dimensional images in the x- and y-dimensions. The images are then stacked in the z-direction. Each column in the three-dimensional array represented by the shaded pixels in Figure 17 is the same pixel position in all images. Each column is then analyzed individually. The intensities of each pixel in each column are plotted as a function of the position of the reference mirror as shown in Figure 8. The phase shift, ψ, of the plot is then put into a two-dimensional array in the location of the pixel. This image analysis process of the images in Figure 17 displays an example of the analysis that will be applied to a set of interference images. The actual phase shift array will be the size as that of the interference images that are analyzed.
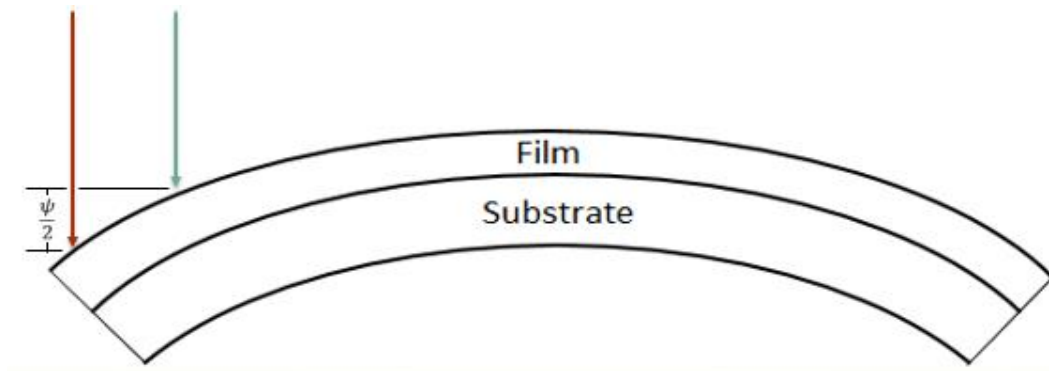

Figure 18: The phase shift relationship to curvature of a thin film-substrate film. The beam paths of neighboring areas shown as red and blue arrows. The curvature of the film-substrate system in this example is related to the path length difference of the adjacent areas.

Figure 18 shows the physical relation of the phase shift between two pixels and the curvature of the film-substrate system. Assuming that the reflected light follows the same path as the incident light (i.e. that the reflected beam is collimated), the additional distance the adjacent pixel's light must travel is ψ. Thus the difference in film height is $\frac{\psi}{2}$. Note, however, that the physical curvature of the film-substrate system would result in the incident beam contacting the surface and reflecting at an angle. This would affect the size of the image, and would alter the phase shift of each pixel. A software correction will eventually be made to account for the effect of this decollimation of the topographical image.

The phase shift-curvature relationship is the basis for using the phase shift between adjacent pixels to create a topographical map. The LabVIEW program will convert the phase shift to a height difference between adjacent pixels by using the wavelength of the laser. For example, if the phase shift between two particles were to be $(1/5)\lambda$, the height difference would be $(1/10)\lambda$ or 63.4 nm.

If the phase shift calculated by the LabVIEW program for a pixel differs by more than $\frac{\pi}{2}$, subtractions of $\frac{\pi}{2}$ will be made until the difference in neighboring pixel phase shifts are less than or equal to $\frac{\pi}{2}$. The periodic nature of the cosine squared function in Eq. 16 will be satisfied for any value of $(\Psi \pm n\pi)$ where n is any integer. The restriction on the difference in the value of Ψ between adjacent pixels is made to produce a smooth surface fit. This is necessary but imposes a limitation that the program can only produce a topographical map that has maximum height changes of $\frac{\lambda}{4}$ per pixel.

The software begins at the center pixel location and compares the phase shift to the neighboring pixels in four directions (+x, -x, +y, -y). The program continues along a single line comparing the phase shift to the neighboring phase shift. This continues in all four quadrants of the image. A result of this method can be a grainy quality of the topographical image.

3.3.4 Substrate Curvature Subtraction

Stresses within the substrate before film deposition may result in the substrate being naturally curved. In addition, non-ideal optics will result in a curved topographical image even if the sample were perfectly flat. A series of interference images are taken before deposition and a topographical map is created. This reference topographical image is subtracted from the film topographical image to create an image whose curvature is solely a result of the stresses within the deposited film and independent of any optical irregularities.

The LabVIEW program will calculate the curvature of the system by fitting the resulting topographical image to a spherical cap. Application of the Stoney Formula can relate the curvature of the topographical map to the stress within the thin film.

36

Chapter 4

RESULTS/ANALYSIS

4.1 Image Set Production

The interferometer produced an interference pattern as a result of the difference in the reference path and the sample path. The combined beam was displayed on the screen, photographed by a webcam, and then processed by a LabVIEW program. LabVIEW automatically output a variable voltage that was amplified by an Op-Amp circuit, which controlled the reference mirror position. As the LabVIEW program moved the mirror resulting in a change in the reference path length, the interference pattern displayed on the screen was captured by the webcam. Figure 19 shows the first 12 images in a set of 19 images taken as the reference mirror moved. Note, that as the reference mirror moves, the intensity of each given pixel changes between dark and light according to Eq. 16. Additionallly, it is important that the physical relationship of the phase shift of adjacent pixels is that $\frac{\psi}{2}$ gives the height of the film surface at the position of that pixel.
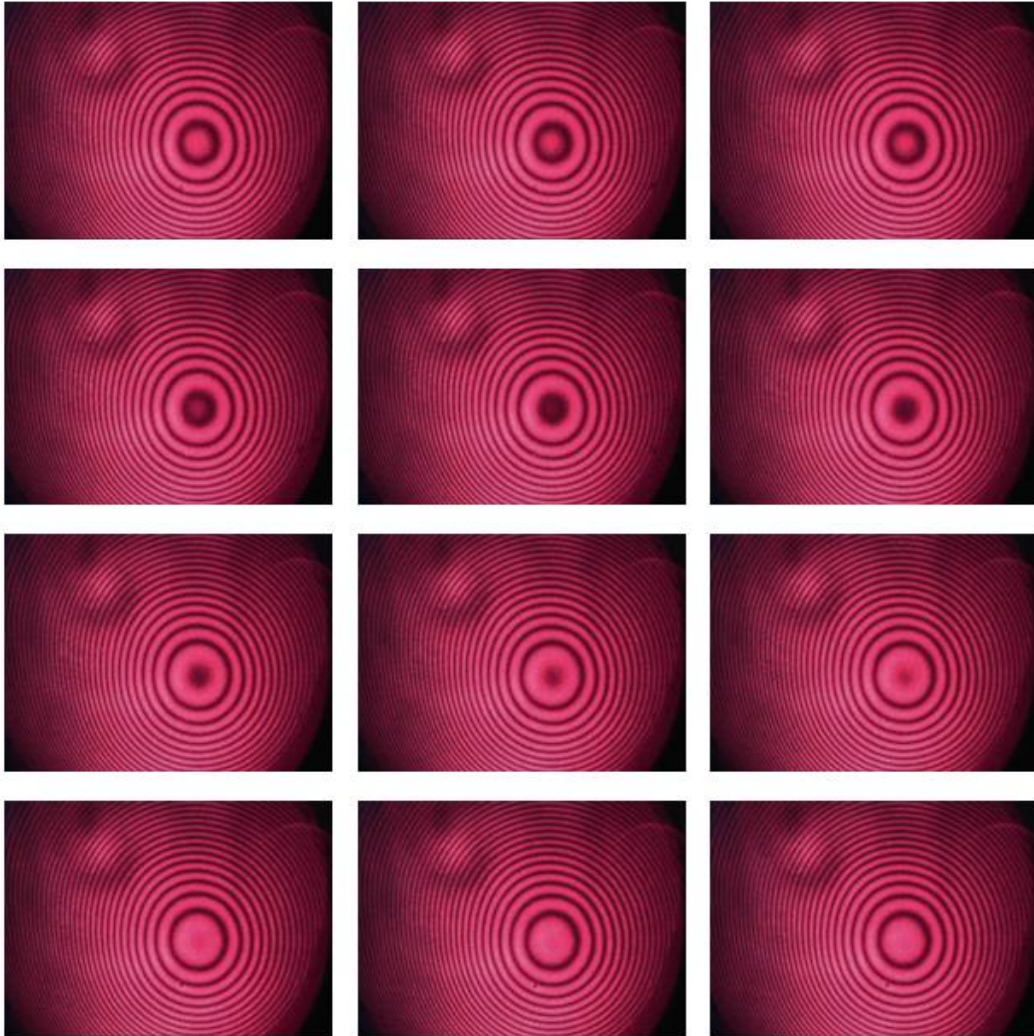
Figure 19: A series of interference patterns taken as the reference mirror moved. This shows 12 images in a set of 19 that were taken automatically using LabVIEW and YAWCAM. The reference mirror moved a total displacement of about 800-900 nm during the total set. Images were taken every second as the LabVIEW program moved the reference mirror. Time progresses from left to right (the first image being the top left, 3rd image being the top right, and the 12th image being the bottom right).

4.2   Image Set Analysis

The set of 19 images, part of which is shown in Figure 19, was analyzed by the LabVIEW program. The topographical map that was produced is shown in

Figure 20. Much like a contour map of a landmass where lines represent areas of equal elevation, the interference patterns can be estimated the same way visually where rings of the same intensity light are like contour lines. The topographical image shown in

Figure 20 is a reference topographical image and thus has not undergone image subtraction. Thus, the image in does not represent the topography of the sample mirror. The images in Figure 19 suggest that near the center of the image there is either a mountain or a valley which slopes toward the edges of the picture. At the edges, especially the corners, where there are not interference patterns, the program fit is as best as possible but the topographical image in those locations is not very meaningful. Upon examination of the topographical image produced by the LabVIEW program, the surface has a valley in the center like we estimated. The grainy look of

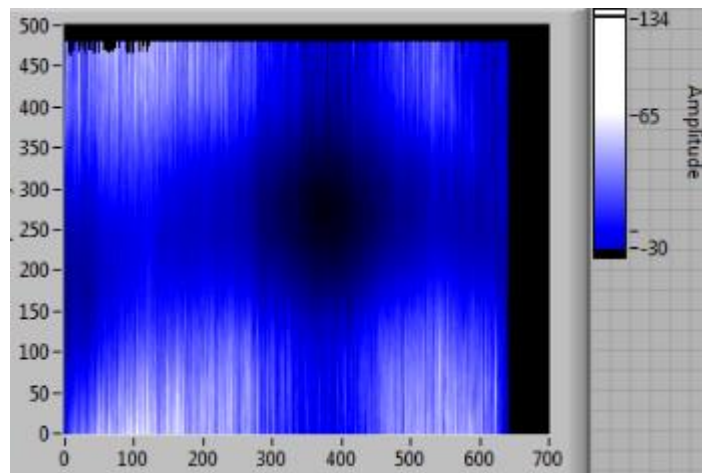Figure 20 is a result of the method the LabVIEW program uses to process the interference pattern images.

Figure 20: Reference Topographical image of sample mirror. The x- and y-axes are the pixels in the x- and y-direction of the topographical image (640x480). The topographical image has the same dimensions as the interference images that were analyzed. The dark color (black) represents area that have lower heights, the lighter color (white) represent areas that are higher, and the shades of blue are in the middle as shown by the arbitrary scale on the right.

CONCLUSIONS

5.1   Current Status

The interferometer in operational to the extent that it can automatically take interference images and process them to produce a topographical image. Currently, when the interferometer is at rest the interferance image displayed on the screen bounces, noticibly due to air currents, building vibrations, and other possible sources of vibrations. Image instability keeps the interferometer from producing the best potential images, thus further work is required to mechanically stabilize the system.

Recently, to stabilize the sample mirror, all of the components mounted on the optics table were shifted such that the sample mirror, which had been mounted overhanging the optics table, could mount directly to the optics table. This change required the removal of the redirection mirror, thus the webcam and screen have been moved off of the optics table to capture the image without a redirection mirror.

To stabilize the overall system, the interferometer has been suspended inside a frame by four dampening springs. These springs are intended to dampen the building vibrations. Additionally, four horseshoe magnets have been implemented as shown in Figure 21 for eddy current dampening. As the aluminum plate passes through the magnetic field of the horseshoe magnet, a current is induced which creates a force opposing the motion of the plate. This happens continually, dampening the oscillations of the system.
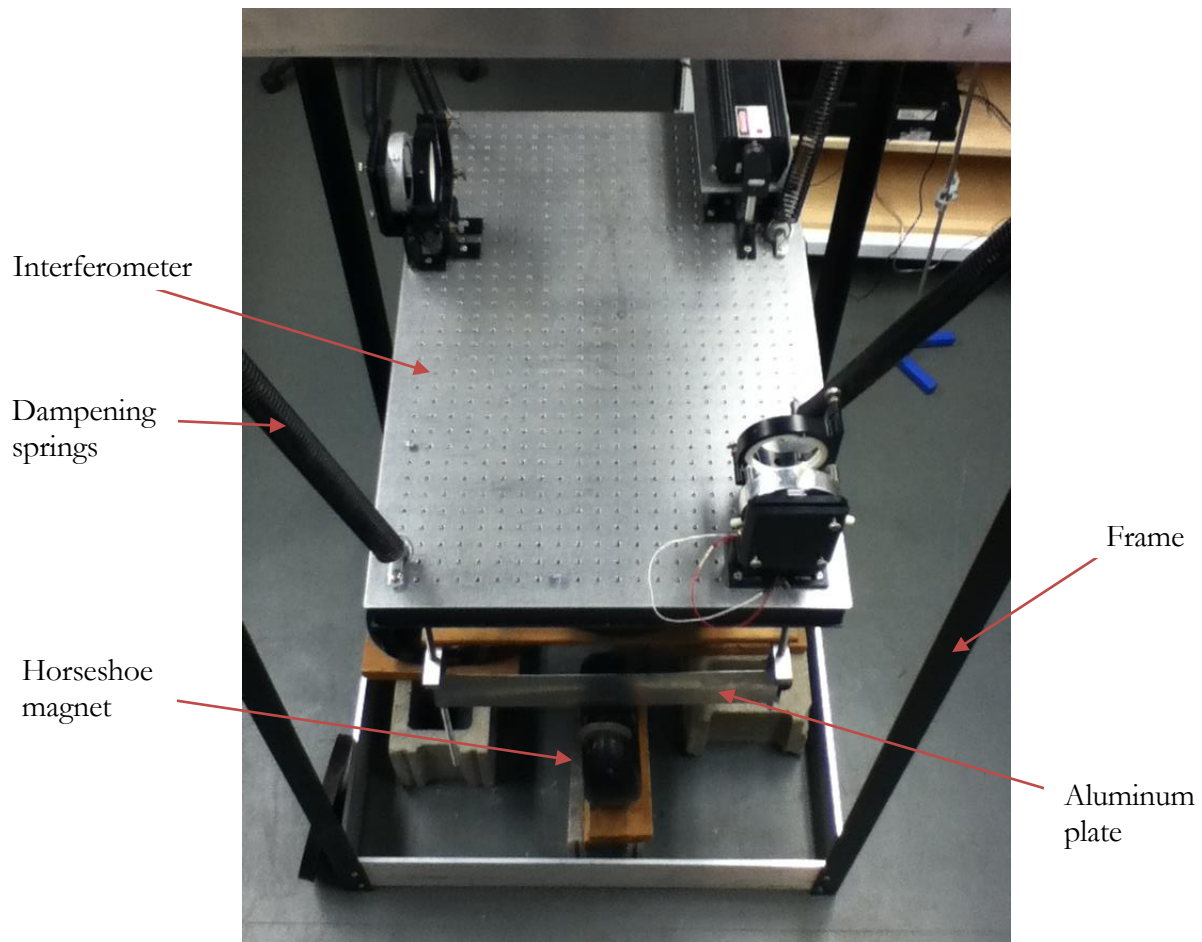
Figure 21: Picture of current status of the interferometer. The interferometer is mounted on an optics table. The frame is holding the interferometer suspended by dampening springs. Four horseshoe magnets are positioned around the base of the frame. Aluminum plates are connected to the underside of the optics table and pass partially through the horseshoe magnets.

5.2   Future Plans

5.2.1   *Image Stabilization*

Image stability is still an issue. Further work will be put into mechanically dampening the system such as securely mounting the horseshoe magnets to the frame to maximize the dampening effort. Additionally, tests can be run to determine which thickness of aluminum plates work best to dampen

the system. The best plate thickness can be used to increase the effectiveness of the eddy current dampening. Lastly, a new smaller laser can be purchased and implemented. The current laser is mounted in such a way as it hangs off the optics table which could be causing some of the vibrations.

5.2.2   In-situ measurements

Once fully operational, the interferometer will be mounted beneath the Houghton College Deposition Chamber as shown in Figure 22. Following the interferometer being mounted underneath the deposition chamber, the sample mirror will be removed and the thin film inside the chamber will reflect the beam instead of the 3 in sample mirror. The interferometer will take a set of interference images and create topographical image of the substrate before a film is deposited as a reference topographical image.

Following the deposition of a thin film on the substrate, another set of images will be taken and a topographical image will be produced. The reference image will be subtracted from the second topographical image to produce a final topographical image of the thin film. This whole process will be done while the sample is under the same conditions it was deposited. This eliminates any changes that could happen between the film being deposited and the film being measured by the interferometer.
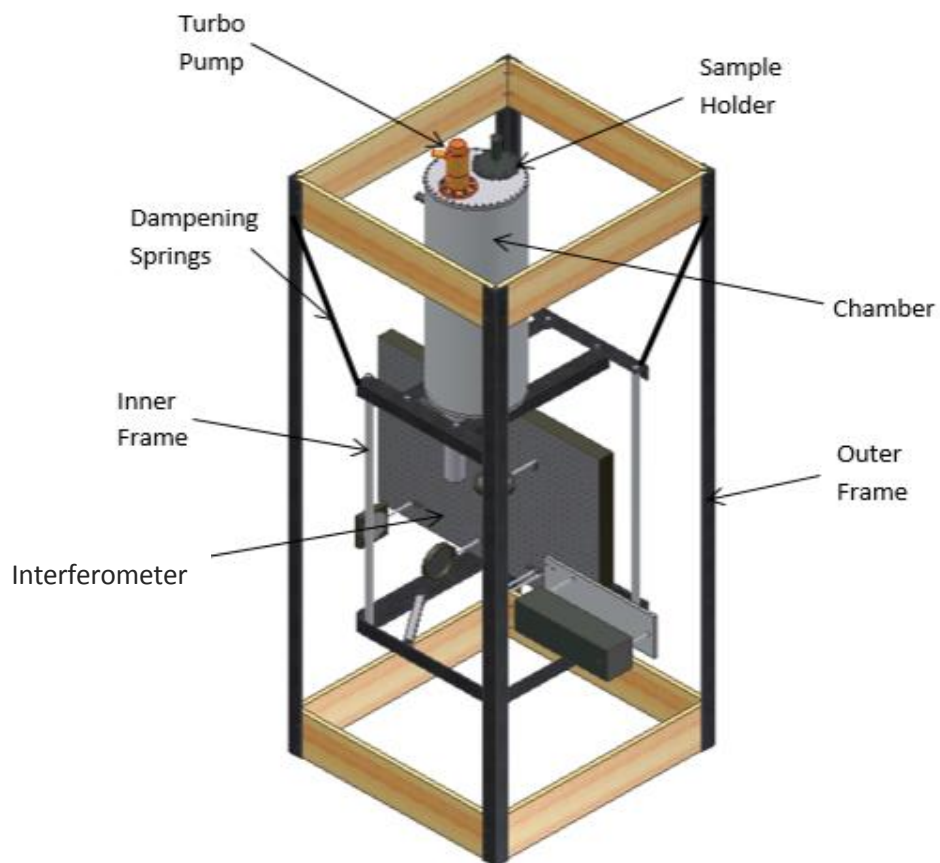
Figure 22: Schematic of the interferometer mounted beneath the deposition chamber. The interferometer-chamber system will be suspended on dampening springs similar to the way it is currently to dampen vibrations. The sample mirror is removed from the interferometer. The sample beam will pass through a window in the bottom of the chamber and contact the sample located at the top of the chamber. In-situ topographical images will be created.

R e f e r e n c e s

[1] L. B. Freund and S. Suresh, Thin Film Materials: Stress, Defect Formation, and Surface Evolution (University Press, Cambridge, 2003), p. 3.

[2] Y. Zoo, D. Adams, J. W. Mayer, T. L. Alford, Thin Solid Films **513**, 170 (2006).

[3] A. Bhandari, B. W. Sheldon, and S. J. Hearne, J. Appl. Phys. **101**, 033528 (2007).

[4] L. B. Freund and S. Suresh, Thin Film Materials: Stress, Defect Formation, and Surface Evolution (University Press, Cambridge, 2003), p. 1-2.

[5] L. B. Freund and S. Suresh, Thin Film Materials: Stress, Defect Formation, and Surface Evolution (University Press, Cambridge, 2003), p. 66-71.

[6] C-C. Lee, C-L. Tien, and J-C. Hsu, Appl. Opt. **41**, **2043** (2002).

[7] L. B. Freund and S. Suresh, Thin Film Materials: Stress, Defect Formation, and Surface Evolution (University Press, Cambridge, 2003), p. 70.

[8] S. P. Baker, B. Hoffman, L. Timian, A. Silvernail, E. A. Ellis, Acta Materialia **61** (2013).

[9] T. Young, Phil. Trans. R. Soc. London **92**, 12 (1802).

[10] T. Young, Phil. Trans. R. Soc. London **94**, 1 (1804).

[11] D.Pogosian, Lecture 32: Two-source interference of light (2010).

[12] A. A. Michelson and E. W. Morley, Philos. Mag. 5 **24**, 449 (1887).

[13] F. Twyman, Trans. Faraday Soc. **16**, 208 (1920).

[14] F. Twyman and A. Green, U. S. Patent 1,252,512 (1918).

[15] F. Twyman, Trans. Opt. Soc. **22**, 174 (1921).

[16] J. H. Bruning, D. R. Herriott, J. E. Gallagher, D. P. Rosenfeld, A. D. White, and D. J. Brangaccio, Appl. Opt. 13, 2693 (1974).

[17] C-C. Lee, C-L. Tien, and J-C. Hsu, Appl. Opt. **41**, **2044** (2002).

[18] A. J. Lewis, Ph.D. thesis, University of London, 1980.

[19] K. Flemington, Undergraduate Thesis (Houghton College, New York, 2015, unpublished).

[20] G. G. Stoney, Proc. R. Soc. A, **82**, 172 (1909).